Journal of
Materials Chemistry B

Materials for biology and medicine

Accepted Manuscript

This article can be cited before page numbers have been issued, to do this please use: X. Chen, J. Zhang, S. Rahimi, K. Kozjek, L. Larsson, I. Mijakovic and S. Pandit, *J. Mater. Chem. B*, 2026, DOI: 10.1039/D6TB00324A.

ROYAL SOCIETY OF CHEMISTRY

rsc.li/materials-b

View Article Online
DOI: 10.1039/D6TB00324A

ARTICLE

Mechanistic insight into graphene coatings for oral biofilm inhibition and osteoblast compatibility

Received 00th January 20xx,
Accepted 00th January 20xx

DOI: 10.1039/x0xx00000x

Xin Chen, [a] Jian Zhang, [a] Shadi Rahimi, [a] Katja Kozjek, [b] Lena Larsson, [c] Ivan Mijakovic, [ad] and Santosh Pandit *[a]

The initial adhesion of bacterial cells to implant surfaces is a critical step in biofilm formation. Biofilms are complex microbial communities that are much more tolerant to conventional antimicrobial treatments than planktonic cells, often requiring mechanical disruption in addition to antimicrobial treatment. Once established, these biofilms and their self-produced extracellular matrix are difficult to eradicate. As a result, there is growing interest in engineering implant surfaces that can effectively disrupt bacterial adhesion and subsequent biofilm formation. Various surface modification strategies, including antimicrobial agents and nanomaterial-based coatings, have been investigated. Among these, graphene-based coatings have shown promising antimicrobial properties. However, mechanisms of their bactericidal activity remain insufficiently understood. This study evaluates the antimicrobial efficacy of vertically aligned graphene (VG) coatings against *Streptococcus mutans*, employing electron microscopy and transcriptomics analysis to elucidate the mode of action. The findings suggest that these coatings inhibit biofilm formation through a multifaceted mechanism: (i) reducing bacterial colonization, (ii) mechanical disruption of bacterial membranes by nanoscale protrusions, and (iii) modulating the expression of genes associated with membrane integrity, transport, oxidative stress, and cell division. Importantly, the coatings inhibited bacterial adhesion and biofilm formation without affecting osteoblast growth or proliferation. These results indicate that VG coatings could offer a dual benefit by enhancing antimicrobial activity while being compatible for osseointegration, indicating their potential as candidates for next-generation biomedical implants.

Introduction

Implant-associated infections (IAIs) present a significant global health challenge, contributing to increased morbidity, mortality, and substantial healthcare costs [1]. The incidence of IAIs can reach up to 30% for certain medical devices [2]. These infections occur when bacteria enter the body through the implant site, adhere to the device surface, and initiate biofilm formation [3]. Biofilms are structured communities of microorganisms encased in a self-produced extracellular matrix, which enables adherence to both biological tissues and inert materials [4, 5]. In IAIs, bacteria colonize the surfaces of implanted medical devices and secrete extracellular polymeric substances (EPS) that form a protective biofilm matrix, which limits the penetration of antibiotics. Additionally, the microcolonies formation and aggregation of bacterial cells within the biofilm facilitates collective defence mechanisms, such as the sharing of tolerant genes and localized inactivation of antimicrobials, further enhancing their resilience [6]. This structure enhances bacterial tolerance to antibiotics and evasion from the host immune system, making IAIs fundamentally more difficult to treat than standard infections [7]. While infections caused by planktonic bacteria generally respond to antibiotic therapy aided by immune defences, biofilm-associated

[a] *Systems and Synthetic Biology Division, Department of Life Sciences, Chalmers University of Technology, SE-412 96, Gothenburg, Sweden. E-mail: pandit@chalmers.se*
[b] *National Bioinformatics Infrastructure Sweden (NBIS), SciLifeLab, Department of Laboratory Medicine, Lund University, Lund, Sweden.*
[c] *Department of Periodontology, Institute of Odontology Sahlgrenska Academy, University of Gothenburg*
[d] *The Novo Nordisk Foundation, Center for Biosustainability, Technical University of Denmark, DK-2800 Kogens Lyngby, Denmark.*
† Footnotes relating to the title and/or authors should appear here.
Supplementary Information available: [details of any supplementary information available should be included here]. See DOI: 10.1039/x0xx00000x

View Article Online
DOI: 10.1039/D6TB00324A

infections often persist due to the protective EPS matrix, as well as reduced bacterial metabolic activity and altered gene expression within the biofilm [7-10].

The rise of antibiotic-tolerance infections represents a major public health challenge worldwide. IAIs are particularly problematic because bacteria can form biofilms on device surfaces, which protect them from antibiotics and the host immune system. These persistent biofilm-associated infections are difficult to treat and often require prolonged therapy or device removal. Preventing bacterial colonization on medical devices is therefore critical, suggesting the need for surface modifications and coatings that can inhibit biofilm formation and improve clinical outcomes. Titanium is one of the most widely used materials for medical implants, valued for its favourable mechanical properties and biocompatibility. However, titanium also has limitations, including a lack of inherent antimicrobial properties. While its surface supports osseointegration, it remains bioinert in terms of preventing bacterial adhesion, making it susceptible to microbial colonization and infection [11].

To overcome these challenges, researchers have developed advanced surface modification strategies to enhance both osseointegration and antimicrobial performance [12]. These include the incorporation of antimicrobial agents such as silver nanoparticles, antimicrobial peptides, and metal ions, as well as the engineering of nanostructured surfaces that simultaneously promote bone cell adhesion and inhibit bacterial growth [13-16]. Such multifunctional coatings aim to improve implant integration with surrounding bone tissue while reducing infection risk, thereby improving long-term implant success. Among these strategies, surface modifications utilizing antibacterial agents such as quaternary ammonium compounds (QACs) are frequently employed for treating infected bone defects [17-19]. Although QACs exhibit strong antimicrobial properties, they often pose a trade-off between antibacterial efficacy and biocompatibility [20]. The positive charge and hydrophobicity of QACs can disrupt mammalian cell membranes, leading to cytotoxic effects [21]. This membrane disruption may also trigger oxidative stress and the generation of reactive oxygen species (ROS), which can damage cellular components, promote inflammation, and impair bone healing [20,21].

An alternative and promising strategy involves mimicking the nanoscale surface structures found on insect wings, such as those of cicadas and dragonflies [22,23]. These natural surfaces contain sharp nanoscale features capable of mechanically rupturing bacterial membranes, thereby preventing bacterial adhesion and biofilm formation without relying on chemical agents. This approach offers a scalable and cost-effective solution for developing antibacterial surfaces on biomedical implants. Hierarchical surface topographies that combine microscale roughness with nanoscale features have been shown to enhance both antibacterial activity and biocompatibility [24,25]. Microscale features aid mechanical interlocking with bone tissue to support osseointegration, while nanoscale structures mimic the extracellular matrix to promote cellular interactions and inhibit bacterial adhesion [26,27]. Titanium implants with such micro/nano-structured surfaces have presented improved osteogenic activity and intrinsic antibacterial properties by tailoring surface topography [28].

In this context, graphene-based coatings with controlled flake density and orientation have recently emerged as a novel approach to deactivate bacterial cells while remaining biocompatible with mammalian cells [29-31]. However, existing studies predominantly focus on early-stage bacterial interactions-often testing antimicrobial activity against non-biofilm-forming strains or after only 24 hours of bacterial growth, a timeframe insufficient for the development of mature, three-dimensional biofilms. Furthermore, the current understanding of graphene's bactericidal activity is largely limited to its mechanical effects namely, membrane disruption by sharp flake edges [29-32]. There remains a significant knowledge gap regarding the comprehensive mechanisms of action, including how such surfaces interact with bacterial cell membranes, intracellular components, and broader metabolic processes.

Despite the growing interest in graphene-coated surfaces for biomedical applications, little is known about their effects on mammalian cells, particularly osteoblasts, which are essential for bone regeneration. We hypothesize that graphene-coated surfaces can inhibit bacterial biofilm formation through direct interactions with bacterial cells while supporting osteoblast growth and proliferation. To test this, the present study investigates the antimicrobial mechanisms of graphene-coated surfaces and evaluates their impact on osteoblast behaviour. *S. mutans*, a well-

View Article Online
DOI: 10.1039/D6TB00324A

characterized oral pathogen known for its robust biofilm-forming ability, was selected as the model organism [33]. This study integrates microbiological, microscopic, and transcriptomic approaches to provide a comprehensive, multiscale understanding of how oriented graphene flakes interact with bacterial cell walls, intracellular components such as nucleic acids, and associated stress response pathways. By simultaneously examining these mechanisms alongside osteoblast behaviour, it offers novel insight into the multifaceted functionality of such surfaces indicating their potential to both inhibit bacterial activity and support bone-forming cells, thereby advancing the design of multifunctional coatings for biomedical implants.

Experimental

Graphene coatings

VG nanoflakes were synthesized via plasma-enhanced chemical vapor deposition (PECVD) using an Aixtron Black Magic system as described previously [29]. Briefly, the substrates consisted of standard p-type silicon wafers coated with a 400 nm layer of silicon dioxide (SiO_2), thermally grown by wet oxidation in an oxyhydrogen atmosphere at 1050 °C. After substrate preparation, the wafers were loaded into a cold-wall CVD chamber and rapidly heated at a rate of approximately 300 °C/min to a growth temperature of 775 °C. Prior to graphene deposition, the substrates were annealed in a reducing atmosphere consisting of hydrogen and argon. Graphene growth was initiated by igniting a 75 W DC glow discharge plasma, using a gas mixture of 15 sccm acetylene (C_2H_2), 15 sccm hydrogen (H_2), and 1000 sccm argon (Ar).

Bacterial growth, biofilm formation and antimicrobial activity evaluation

The antimicrobial efficacy of graphene-coated surfaces was assessed using *Streptococcus mutans* UA159. Bacterial cultures were grown in brain heart infusion (BHI) broth supplemented with 1% glucose, incubated at 37 °C in a humidified atmosphere containing 5% CO_2. To prepare the bacterial inoculum for testing, overnight cultures were diluted in 1% sucrose BHI broth to achieve a final concentration of approximately $2–5 \times 10^6$ CFU/mL. A volume of 50 µL of this inoculum was carefully dispensed onto each sample surface, including both control and graphene-coated substrates, and incubated under the same conditions for 24 hours. Following this initial incubation, the medium was replaced with fresh 1% sucrose BHI broth, and incubation was continued for an additional 24 hours. Notably, to prevent evaporation of the culture medium from the sample surfaces, the tested samples were placed in the middle part of a 24-well plate, while the surrounding wells and inter-well spaces were filled with sterilized distilled water.

After 48 hours of total incubation, biofilms formed on the surfaces were gently rinsed twice with sterile distilled water and transferred into 5 mL of 0.89% NaCl solution. Biofilms were then dislodged and homogenized using probe sonication at 10 W for 30 seconds, repeated three times. The resulting suspensions were serially diluted and plated onto BHI agar. Colony-forming units (CFUs) were enumerated after 48 hours of incubation, and the percentage reduction in viable bacteria was calculated relative to the control samples. All experiments were performed in triplicate, and standard deviations represent variation across biological replicates.

Scanning electron microscopy analysis

For scanning electron microscopy (SEM) analysis, 48-hour biofilms grown on both control and graphene-coated surfaces were fixed in 3% glutaraldehyde for 2 hours. Samples were then dehydrated through a graded ethanol series (40%, 50%, 60%, 70%, 80%, and 90% v/v, each for 10 minutes), followed by a final dehydration step in 100% ethanol for 20 minutes. Dehydrated samples were air-dried at room temperature for 2 hours. Prior to imaging, a 5 nm gold coating was applied to each sample. SEM imaging was performed using a Supra 60 VP instrument (Carl Zeiss AG). Three independent biological replicates were analysed for each condition, with five representative fields imaged per replicate.

Confocal laser scanning microscopy analysis

Confocal laser scanning microscopy was used to examine the extent of live/dead bacterial cells and EPS production by bacterial cells on VG coated and non-coated surfaces. The 48-h-old biofilms were stained at room temperature in the dark for 30 min using 6.0 µM SYTO 9 and 30 µM propidium iodide (LIVE/DEAD BacLight bacterial viability kit L13152, Invitrogen, Molecular Probes, Inc. Eugene, OR, USA). CLSM imaging of the biofilms was performed using the Nikon A1 equipped with argon-ion and helium–neon lasers. The

View Article Online
DOI: 10.1039/D5TB00334A

excitation wavelengths for SYTO 9 and propidium iodide are 488 and 543 nm, respectively. Three independent experiments were performed and five image stacks per experiment were collected (n = 10). The bio-volume of live and dead cells was quantified from the entire stack using the COMSTAT image-processing software (Heydorn et al, 2000; Pandit et al, 2013). The bio-volume is defined as the volume of the biomass (μm^3) divided by the substratum (SiO_2 surface) area (μm^2).

To examine the EPS and bacterial cells within the biofilm matrix, EPS matrix and bacteria were stained as described previously [33]. Briefly, 1 µM of Alexa fluor® 647-labeled dextran conjugate was added to the culture medium during the biofilm growth to stain exopolysaccharides. After 48 h these biofilms were exposed to 2.5 µM SYTO® 9 green-fluorescent nucleic acid stain. Two independent experiments were performed and 5 image stacks (512 × 512 pixel) from 5 sites per experiment were collected (n = 10). Biofilms (bacterial bio-volume and thickness, and EPS bio-volume and thickness) were quantified from the confocal stacks by using COMSTAT [34].

To assess intracellular reactive oxygen species (ROS), bacterial cells cultured on control and VG-coated surfaces were stained with CellROX™ Deep Red Sensor (Life Technologies) and DAPI. The cells were first incubated with CellROX™ Deep Red dye for 20 minutes, followed by counterstaining with DAPI for an additional 20 minutes. Excess dye was removed by washing with sterile water, and the samples were then observed using a fluorescence microscope (Zeiss, Axio Imager Z2m).

Transcriptome analysis

Approximately 2×10^7 bacterial cells were harvested at 14,000 × g and rapidly froze to minimize mRNA degradation. Total RNA was extracted using the RNeasy Mini Kit (GIAGEN, Germany) following the manufacturer's instructions. Cells were disrupted with a FastPrep homogenizer (MP Biomedicals, USA), and genomic DNA was removed using DNase I (Invitrogen, USA). RNA concentration and integrity were determined with the Qubit RNA HS assay kit (Thermo Fisher Scientific, USA) and the Agilent 2100 bioanalyzer (Agilent Technologies, USA), respectively. RNA-seq was performed at the National Genomics Infrastructure (NGI) of SciLifeLab, Sweden. The raw RNA-seq data are available in the Genome Expression Omnibus (GEO) database (https://www.ncbi.nlm.nih.gov) under BioProject ID: PRJNA1390808.

RNA sequencing data was analysed using a Nextflow based nf-core/rnaseq pipeline (version 3.12.0, 35,36) along with a custom written Snakemake workflow. Within the nf-core/rnaseq pipeline, FastQC was used to assess the quality of the raw FastQ files. Adapter and quality trimming were performed using Trim Galore (https://www.bioinformatics.babraham.ac.uk/projects/trim_galore/). Sequencing reads were then aligned to the reference genome of *S. mutans* UA159 using the STAR RNA-seq aligner (37). The resulting BAM alignment files were further processed with the custom Snakemake pipeline. Finally, gene-level counts taking into account only coding sequence (CDS) features were obtained using *featureCounts* (38).

The downstream analysis of the RNA sequenced expression data was carried out in R (version 4.3.3). The matrix of the expression data was normalized using the variance stabilizing transformation (VST) implemented in DESeq2 (39) to account for library size differences and within-group variability of low counts. A principal component analysis (PCA) of the normalized expression data was performed to visualize sample clustering and assess similarity/dissimilarity in expression profiles. Differential gene expression analysis was conducted using DESeq2 (39). Genes with an adjusted *p*-value below 0.05 ($p_{adj} < 0.05$) were considered significantly differentially expressed. These results were visualized using volcano plots. Functional enrichment analysis of differentially expressed (upregulated and downregulated) genes was performed using the enrichR package that provides an interface to the Enrichr database (40). We selected a Gene Ontology (GO) database, and all differentially expressed genes were assessed across three categories: biological process (BP), cellular component (CC), and molecular function (MF).

Osteoblast cell growth

MG63 osteosarcoma cell line (Middlesex, UK) and human osteoblast cells (HOB-c) were used for toxicity studies. HOB-c was purchased from Sigma. MG63 cells were cultured in Minimum Essential Medium Eagle (Thermo Scientific) supplemented with 10 % fetal bovine serum (Thermo Scientific). HOB-c cells were cultured in osteoblast growth medium (Sigma). Cells were maintained at 37 °C in a humidified atmosphere with 5% CO_2. Control and VG-coated surfaces were placed in 24-well and 48-well plates and seeded with 8×10^4 and 5×10^4 MG63 and HOB-c cells per well, respectively. The

View Article Online
DOI: 10.1039/D6TB00324A

cells were then incubated for 48 hours to allow for adhesion and proliferation. After incubation, cells were treated with a medium containing 1X Alamar Blue (Thermo Scientific) staining solution for 4 hours. Fluorescence was measured using an OPTIMA BLUE Fluostar plate reader (BMG Labtech, Ortenberg, Germany), and results were normalized against the control.

For SEM, after the cell growth for 48 h, samples were fixed using 2.5% of glutaraldehyde for 2 h followed by the dehydration with graded series of ethanol (40%, 50%, 60%, 70%, 80%, 90% and 100%) for 10 min each. The dehydrated samples were dried in room temperature for overnight. The dried samples were sputter coated with gold (5nm) before imaging with SEM.

Statistical analysis

All experiments were conducted in biological triplicates, and data are presented as the mean ± standard deviation (SD). Statistical significance was assessed using a one-way analysis of variance (ANOVA), followed by a post hoc multiple comparison (Tukey test). Unless otherwise specified, biological triplicates were analysed. Statistical significance was defined as $p < 0.05$, unless stated otherwise.

Results and discussion

Graphene coatings and characterization

The synthesis of VG structures via plasma-enhanced chemical vapor deposition (PE-CVD) on various substrates has been established in prior studies. For antimicrobial applications, densely packed arrays of VG nanoflakes are essential to effectively disrupt adhered bacterial cells. Previous research has established that the density, distribution, and height of these nanoflakes are critical parameters that enable physical penetration of bacterial cell walls, leading to the leakage of intracellular contents and subsequent cell deactivation.

Scanning electron microscopy (SEM) at different magnifications indicated the successful formation of a VG coating on the SiO_2 substrate (Fig. 1A and 1B). The low-magnification SEM image showed a uniform surface coverage within the observed field of view, while the higher-magnification image depicts a closely packed nanoflake morphology with abundant edge-like features. An additional top-view SEM image is provided in Fig. S1A. These observations indicate that the substrate surface was covered by a continuous and nanostructured VG layer. Cross-sectional SEM further showed a continuous VG coating with a vertically oriented nanoflake-like architecture on the substrate (Fig. S1B), providing direct structural evidence for VG growth and additional information on the coating architecture. Further morphological characterization by atomic force microscopy (AFM) showed the nanoscale topography of the VG coating (Fig. 1C). Quantitative AFM analysis showed that the surface exhibited a mean roughness (Sa) of 20.67 nm over a scan area of 10 × 10 μm², suggesting the rough and nanostructured nature of the coating. Additional three-dimensional AFM topography is provided in Fig. S1C.

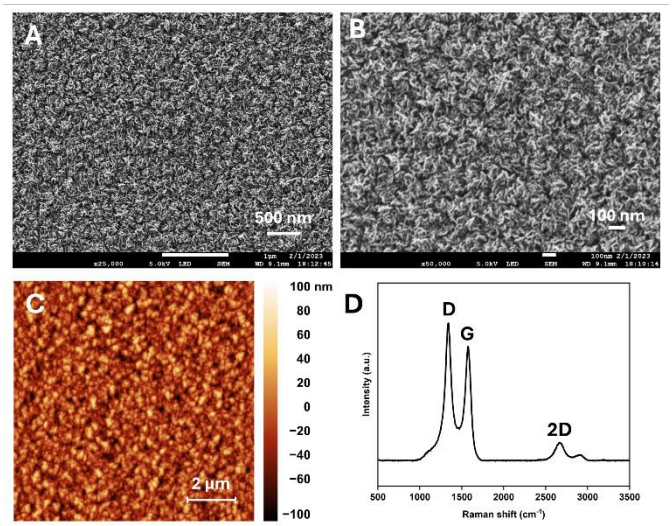

Figure 1. Physicochemical characterization of the VG coating on the SiO_2 surface. (A-B) SEM images of VG coatings on SiO_2 surface from low to higher magnification; (C) Representative 2D AFM topography image the VG coating; (D) Raman spectrum of the VG coating showing the characteristic D, G, and 2D bands.

Raman spectroscopy further showed the graphitic nature of the coating by showing the characteristic D, G, and 2D bands of graphene (Fig. 1D). The D band at approximately 1350 cm^{-1} indicates the presence of structural defects or disorder within the graphene lattice, which is expected for VG due to the high density of exposed edges and grain boundaries. The G band at approximately 1590 cm^{-1} corresponds to the in-plane vibrational mode of sp^2-bonded carbon atoms and is a characteristic feature of graphitic carbon. The relatively high intensity of the D band compared to the G band is

consistent with the vertical structure and the high density of flake boundaries and defects. A small 2D peak at approximately 2650 cm^{-1} was also observed, which is consistent with the presence of multilayer graphene structures. Taken together, the SEM, cross-sectional SEM, AFM, and Raman results indicate the successful formation of a graphitic VG coating with a rough and densely nanostructured surface.

VG coatings protect from *S. mutans* colonization and biofilms growth

Research indicates that microbial colonization of dental biofilms follows a similar pattern on both natural teeth and dental implant surfaces [41]. Among the initial colonizers, *S. mutans* plays a prominent role due to its strong adhesive capabilities. Early colonizers such as *S. mutans*, *Actinomyces spp.*, and *Streptococcus sobrinus* contribute to the initial stages of biofilm formation by facilitating the attachment and growth of more virulent, periodontopathogenic bacteria, including *Porphyromonas gingivalis* and *Treponema denticola* [42]. Unlike natural teeth, dental implants lack anatomical niches that support bacterial attachment, making the role of early colonizers particularly *S. mutans* in initiating biofilm formation on implant surfaces [43].

Due to this fact, *S. mutans* was selected to evaluate the antimicrobial efficacy and mode of action of VG nanoflake-coated surfaces. The impact of VG on bacterial adhesion and growth was assessed by comparing VG-coated and uncoated control surfaces. After 48 hours of incubation, the viability of *S. mutans* on VG-coated surfaces was reduced by 86.1 ± 8.2%, indicating a strong antimicrobial effect (Fig. 2A). This reduction is consistent with previous findings, where viability reductions of 90% and 70% were observed for another Gram-positive bacterium, *Staphylococcus epidermidis*, after 24 and 72 hours of growth on VG-coated surfaces, respectively [29].

In this study, *S. mutans* was cultured in the presence of 1% sucrose to promote adhesion and extracellular matrix production. The glucosyltransferase enzyme produced by *S. mutans* converts dietary sucrose into sticky glucans, which enhance surface adhesion, support co-adhesion of additional pathogenic strains, and contribute to the formation of exopolysaccharide-rich microcolonies [44]. Thus biofilm-promoting condition was used to better simulate in vivo biofilm development and to assess the real-world antimicrobial potential of VG-coated surfaces.

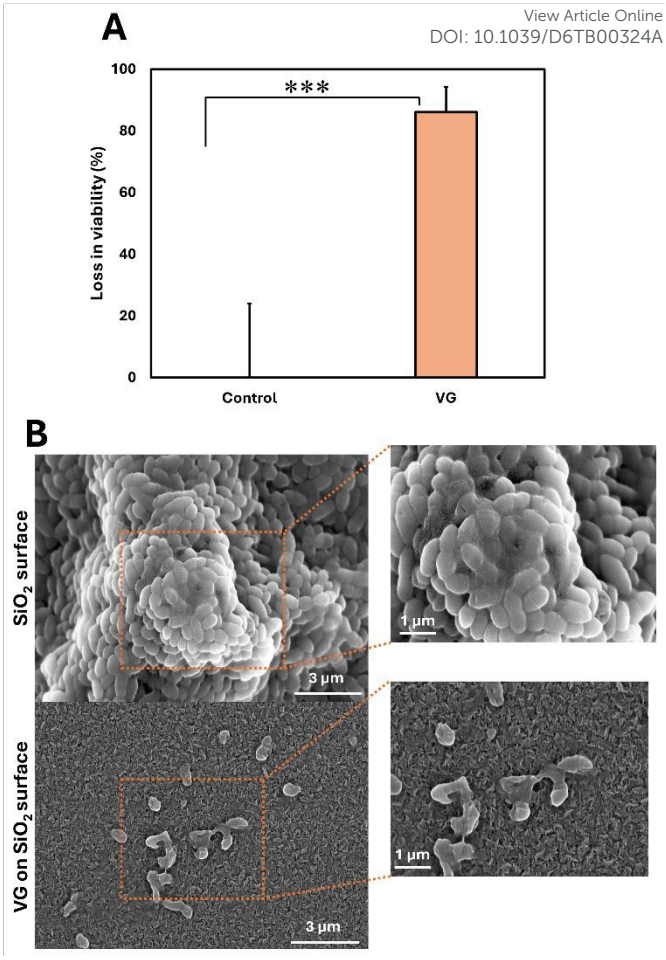

Figure 2. Antimicrobial efficiency of VG coating against *S. mutans*. Viability of bacterial cells (%) on the control and VG surfaces (A). SEM images depicting the biofilm growth and bacterial cell morphology in control (SiO_2) and VG coated surface (B). Data represent mean ± standard deviation of three individual experiments. ***$p < 0.0001$.

To further investigate the extent of bacterial adhesion and the physical interactions between bacterial cells and VG surfaces, both control and VG-coated samples were examined using SEM after 48 hours of *S. mutans* growth. As expected, the control surfaces exhibited dense, three-dimensional biofilm structures with high bacterial cell accumulation (Fig. 2B). In contrast, VG-coated surfaces showed markedly reduced bacterial colonization (Fig. 2B). Moreover, many of the adhered bacterial cells appeared partially or fully ruptured, likely due to mechanical damage caused by the sharp, exposed edges of the VG nanoflakes (Fig. S2).

This physical disruption is consistent with previous reports indicating the bactericidal effect of nanostructured surfaces against a variety of bacterial

View Article Online
DOI: 10.1039/D6TB00324A

pathogens through similar mechanisms [29-31]. Notably, even under biofilm-promoting conditions where *S. mutans* was cultured in the presence of 1% sucrose to enhance adhesion and EPS production, the VG-coated surfaces significantly inhibited both bacterial attachment and accumulation. These observations indicate the potential of VG coatings to effectively prevent biofilm formation on implant surfaces.

To assess bacterial viability more precisely, live/dead staining was performed after 48 hours of growth, followed by confocal laser scanning microscopy. On control surfaces, most bacterial cells remained viable, with relatively few cells stained by propidium iodide (PI), which selectively labels cells with compromised membranes (Fig. 3A). In contrast, a substantial number of *S. mutans* cells adhered to VG-coated surfaces were stained with PI, indicating a high degree of membrane disruption and cell death (Fig. 3A). To quantify these effects, confocal images were analysed to determine the total biomass and thickness of both live and dead cells within the biofilm matrix (Fig. 3B–E). The biovolume of live cells was significantly reduced on VG-coated surfaces compared to controls (Fig. 3B), while the biovolume of dead cells showed a corresponding increase (Fig. 3C). Similarly, the thickness of live cell populations within the biofilm matrix was significantly lower on VG surfaces (Fig. 3D), whereas the thickness of dead bacterial layers was notably higher (Fig. 3E) relative to control surfaces. These findings from live/dead staining are consistent with the SEM observations and bacterial viability assays, collectively indicating the strong antimicrobial and anti-biofilm properties of VG-coated surfaces against *S. mutans*.

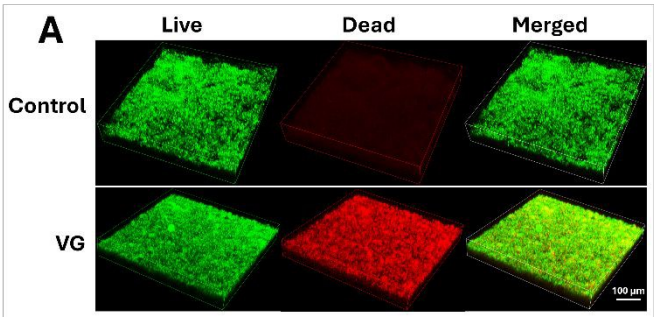

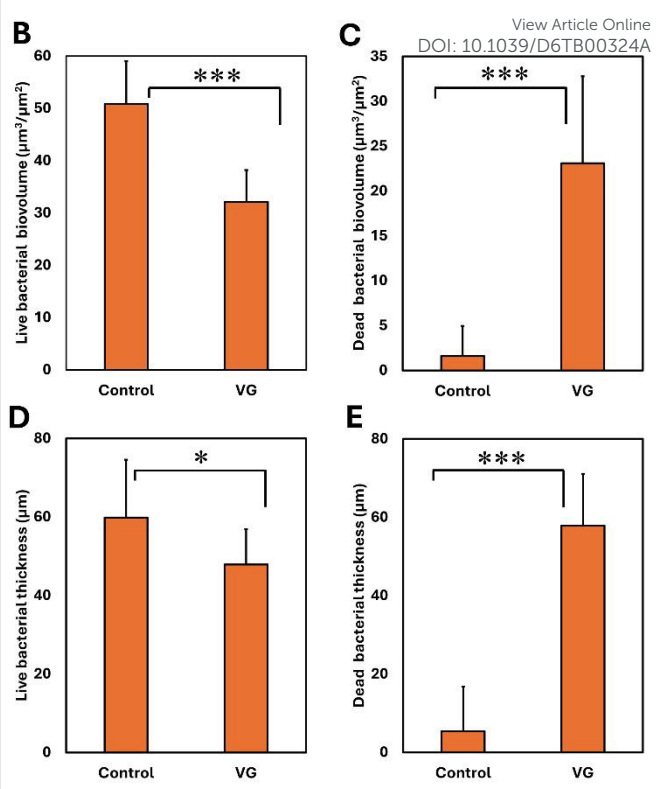

Figure 3. CLSM analysis of live and dead bacterial cells. Representative 3D confocal microscopy images depicting the density of live and dead cells on control and VG coated surface (A). Quantitative analysis of confocal stack images showing biovolume of live and dead cells (B and C). The thickness of live and dead bacterial cells in biofilm matrix (D and E). Data represent mean ± standard deviation of two individual experiments. *$p < 0.05$; ***$p < 0.0001$.

Despite the significant bactericidal activity of VG-coated surfaces, a residual layer of live bacterial cells and limited biofilm formation was still observed. This suggests that a subset of adhered *S. mutans* cells remained viable and may have produced extracellular polysaccharides (EPS), which facilitated co-adhesion and the formation of bacterial aggregates. To evaluate EPS production on both coated and uncoated surfaces, the biofilms were stained using fluorescent markers targeting both polysaccharides and nucleic acids, followed by confocal laser scanning microscopy. As shown in Fig. 4A, the VG-coated surfaces exhibited a markedly reduced EPS signal compared to the uncoated controls, where bacterial cells were embedded in a well-developed EPS matrix. To quantitatively assess the extent of bacterial adhesion and EPS production, the biovolume and thickness of both bacterial cells and EPS were quantified from confocal z-stack images. Consistent with the live/dead staining results, both the

View Article Online
DOI: 10.1039/D6TB00324A

biovolume and thickness of bacterial cells were significantly reduced on VG-coated surfaces compared to the control (Fig. 4B and 4D). Similarly, EPS formation was significantly diminished on the VG-coated surfaces, as indicated by the lower EPS biovolume and thickness within the biofilm matrix (Fig. 4C and 4E). These findings suggest that the antimicrobial effect of VG coatings not only prevent bacterial attachment but also inactivate adhered cells, thereby suppressing metabolic processes essential for EPS production. Since glucosyltransferase (GTF) enzyme is responsible for synthesizing glucan from dietary sucrose is produced by metabolically active *S. mutans* cells, any disruption to adhesion or metabolic function directly limits the production of polysaccharides necessary for mature biofilm development [45, 46].

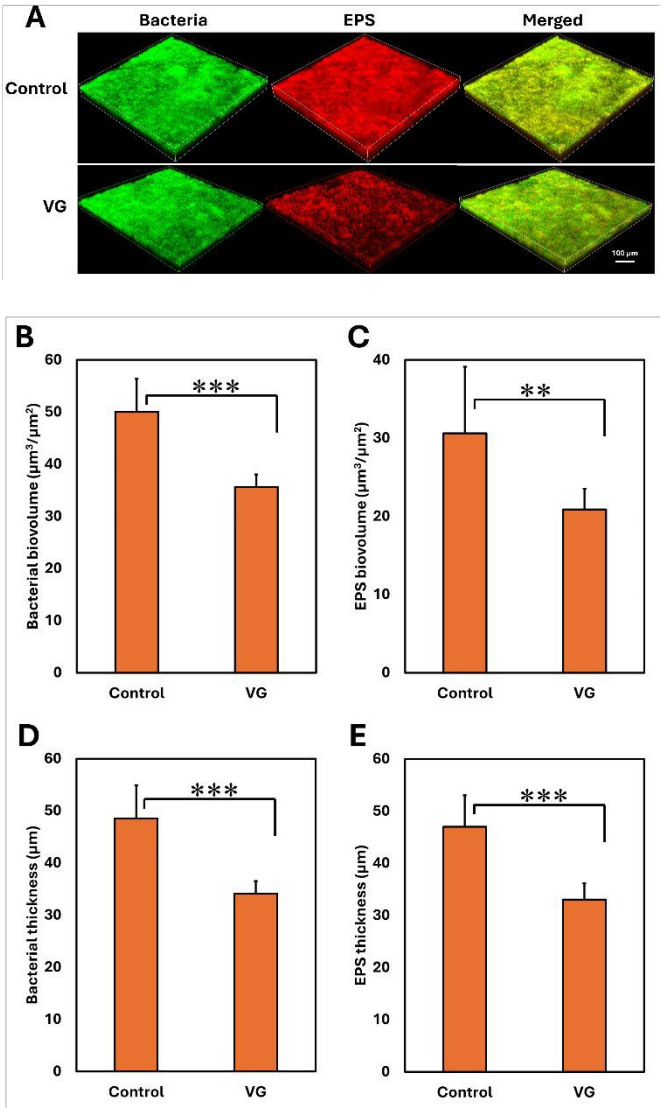

Figure 4. CLSM analysis for bacterial and EPS content in biofilm matrix. Representative 3D confocal microscopy images depicting the density and distribution of bacterial cells and EPS on control and VG coated surface (A). Quantitative analysis of confocal stack images showing biovolume of bacteria and EPS matrix (B and C). The thickness of bacteria and EPS matrix in biofilms (D and E). Data represent mean ± standard deviation of two individual experiments. $^{**}p < 0.005$; $^{***}p < 0.0001$.

VG coatings significantly alter the gene expression of adhered bacterial cells

To gain a comprehensive understanding of gene expression alterations in *S. mutans* grown on VG-coated surfaces, transcriptomic analysis was performed on bacterial cells from three groups: planktonic cultures (M), cells adhered to uncoated control (SiO_2) surfaces (C), and cells adhered to VG-coated surfaces (S). Principal component analysis (PCA) indicated that *S. mutans* cells on VG-coated surfaces (S) exhibited a distinct gene expression profile compared to both planktonic cells (M) and those grown on control surfaces (C) (Fig. S3).

To quantify the extent of transcriptional changes, differential gene expression analysis was conducted between each group. When comparing control surface-adhered cells (C) to planktonic cells (M), a total of 678 genes were differentially expressed (Fig. S4), with 314 genes upregulated and 364 genes downregulated. In comparison, *S. mutans* cells adhered to VG-coated surfaces (S) showed differential expression of 540 genes relative to those on control surfaces (C) (Fig. 5A), including 233 upregulated and 307 downregulated genes. When VG-adhered cells (S) were compared directly to planktonic cells (M), a total of 899 genes were differentially expressed (Fig. 5B), comprising 441 upregulated and 458 downregulated genes. Notably, cells grown on VG-coated surfaces exhibited the significant numbers of differentially expressed genes in compared planktonic cells and cells grown on control surface (Fig. 5), indicating the strong transcriptomic response elicited by the nanomaterial. This supports the hypothesis that VG nanostructures exert their antimicrobial effects through a combination of physical and biochemical interactions.

View Article Online
DOI: 10.1039/D6TB00324A

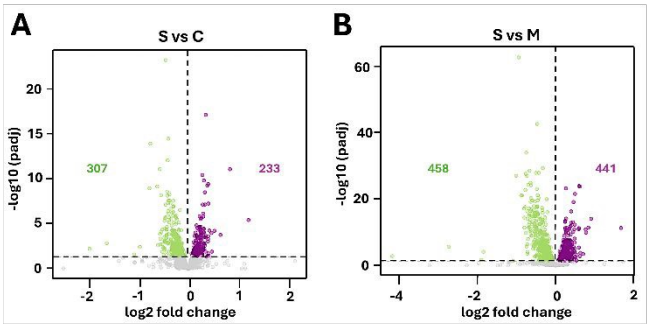

Figure 5. Volcano plot depicting differentially expressed genes level in *S. mutans* cells in VG coated surface in compared to control surface (A) and *S. mutans* cells in VG coated surface in compared to planktonic cells (B). The horizontal black dotted line represents significance threshold at *p*-adj < 0.05.

Differentially expressed genes (DEGs) were further analysed to identify shared expression patterns across the experimental groups (Fig. 6 and Fig.S5). The analysis focused on genes with potential functional relevance in key cellular processes, including membrane transport, cell membrane biosynthesis, cell division, oxidative stress response, and primary metabolic pathways. Among these categories, genes associated with membrane transport and membrane biosynthesis showed the most pronounced differential regulation, followed by those involved in central metabolism, oxidative stress mitigation, and cell cycle progression. Comparative transcriptomic analysis showed a core set of 366 DEGs found to be common in cells grown on VG-coated surface (S) versus cells grown on control surface (C) and cells grown on VG-coated surface (S) versus planktonic *S. mutans* cells (M) (Fig. 6). Within this shared set, 44 genes were linked to transport mechanisms, 19 to cell membrane biosynthesis, 1 to cell division, 15 to oxidative stress responses, and 22 to primary metabolic functions. These findings are consistent with the known antimicrobial mechanisms of graphene-based materials, which are proposed to disrupt bacterial membranes, impair nutrient and ion transport systems, and induce oxidative stress, ultimately leading to microbial inhibition or inactivation [31, 32].

In the context of mechano-bactericidal activity, hydrophobic nanospikes such as VG physically interact with bacterial membranes, disrupting phospholipid alignment and facilitating membrane penetration or lipid extraction [47, 48]. This interaction can lead to pore formation and loss of membrane integrity. Since the bacterial cell membrane contains essential molecular machinery involved in processes such as nutrient transport, metabolite exchange, and cell division, its disruption can cause leakage of intracellular contents and functional collapse [47, 48]. Furthermore, membrane damage is known to trigger excessive production of reactive oxygen species (ROS), resulting in oxidative stress [49]. This redox imbalance can further impair various metabolic and regulatory pathways, contributing to the loss of bacterial viability and function [49, 50]. The combined mechanical and oxidative stress responses observed in this study suggest a multifaceted mechanism of action for VG coatings, supporting their potential use in preventing bacterial colonization and biofilm formation on biomedical surfaces.

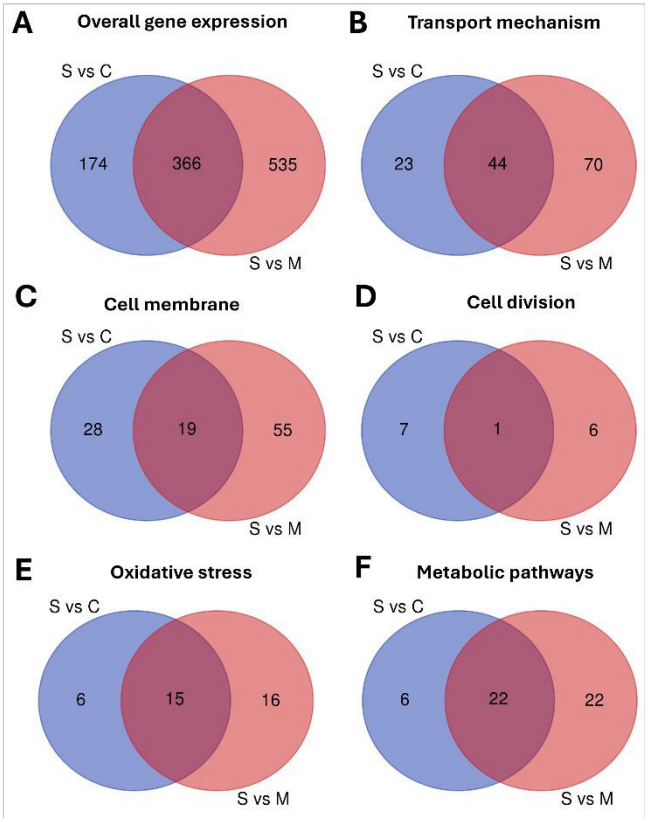

Figure 6. Venn diagram depicting intersection of data – overlap of significantly regulated all genes (A), genes involved in transport mechanism (B), genes associated to cell membrane (C), genes associated to cell division (D), oxidative stress (E) and genes involved in metabolic pathways (F) between the *S. mutans* cells grown VG-coated surface versus cells grown on control surface and cells on VG-coated surface versus planktonic *S. mutans* cells.

Gene Ontology (GO) term analysis of transcriptomic data indicated that several carbon metabolism

View Article Online
DOI: 10.1039/D6TB00324A

pathways in *S. mutans* were significantly affected when cells were grown on VG-coated surfaces (S) compared to those grown on control surfaces (C) (Fig. S6). In broader comparisons such as VG-coated (S) versus planktonic cells (M), a wider range of metabolic pathways found to be affected. This observation aligns with previous studies suggesting that bacterial cells within biofilms exhibit markedly different metabolic states and priorities compared to their planktonic counterparts [51, 52]. To further explore functional changes, DEGs were categorized based on their roles in key cellular processes and compared across all sample groups (Fig. 7 and Fig. S7). Notably, a distinct subset of genes was significantly upregulated in *S. mutans* cells on VG-coated surfaces compared to control surfaces, indicating specific transcriptional adaptations to the nanostructured environment.

The schematic illustration on interaction of VG-coatings to *S. mutans* cells and differentially affected cellular pathways are illustrated in Fig. 8. Among the upregulated genes, *thiT* (involved in thiamine transport) and *atpA* (encoding a subunit of the ATP synthase complex) suggest enhanced nutrient uptake and energy production [52, 53]. Although specific upregulation of *celB*, *treP*, *lacG*, and *treC* in *S. mutans* biofilms has not been directly reported, related systems, such as tagatose metabolic genes (*lacABCD*, *lacG*) show elevated expression in persister cells [54]. This supports the underlying premise of enhanced carbohydrate transport and metabolism associated stress responses [54]. The upregulation of *ftsZ*, a key gene regulating cell division, suggests potential stress for enhanced proliferation [55, 56]. Additionally, genes linked to stress response and cell envelope maintenance such as *yaaA*, *mdeA*, *lytR*, and *macP* were elevated [57- 59]. Broader metabolic reprogramming was suggested by the upregulation of *gltB* (nitrogen metabolism), *carB* (pyrimidine biosynthesis), *galE* (galactose metabolism), and *citC* (citrate metabolism). These changes may reflect increased metabolic flexibility in response to the VG-coated surface, potentially indicating that *S. mutans* cells are adjusting to altered or stressful conditions.

Conversely, a substantial number of genes were significantly downregulated in *S. mutans* cells on VG-coated surfaces. This includes key regulators of cell morphology and division, such as *ftsX*, *mreC*, *gpsB*, and *mltG*, suggesting disruptions in cell wall synthesis and structural maintenance [60-62]. The repression of *spaP*, a major surface adhesin, indicates reduced potential for adhesion and biofilm formation [63]. Additionally, downregulation of genes involved in protein translocation (*secA*) and oxidative stress response—*ahpC*, *sodA*, *tpx*, *mdaB*, *trxA*, and *gorA* may suggest a possible alteration in redox homeostasis and reduced capacity to manage oxidative stress [64,65]. To verify oxidative stress-associated changes, intracellular ROS levels in bacterial cells grown on control and VG-coated surfaces were examined using CellROX Deep Red staining. Cells grown on the VG-coated surface exhibited markedly enhanced CellROX fluorescence compared with those grown on the control surface, indicating increased oxidative stress induced by the VG coatings (Fig. S8). Although oxidative stress-response genes are typically upregulated under such conditions, their downregulation here may reflect a dysregulated or non-canonical stress response, potentially contributing to ROS accumulation. Further, genes associated with DNA repair (*mutM*), central carbon metabolism (*gap*, *gdhA*, *alsS*, *manA*), and glycogen biosynthesis (*glgB*) were also suppressed, which may indicate a possible reorganization of metabolic priorities [66,67]. Downregulation of the global metabolic regulator ccpA may be consistent with a broader shift in carbon metabolism [68]. Finally, reduced expression of *mubX*, *mubY*, and *lpdA* suggest a possible downregulation of pathways associated with energy production, cell envelope integrity, and stress response.

Taken together, this gene expression profile may reflect a multifaceted response by *S. mutans* to the VG coated surface, potentially involving metabolic reprogramming, altered energy expenditure, and modulation of stress response pathways.

View Article Online
DOI: 10.1039/D6TB00324A

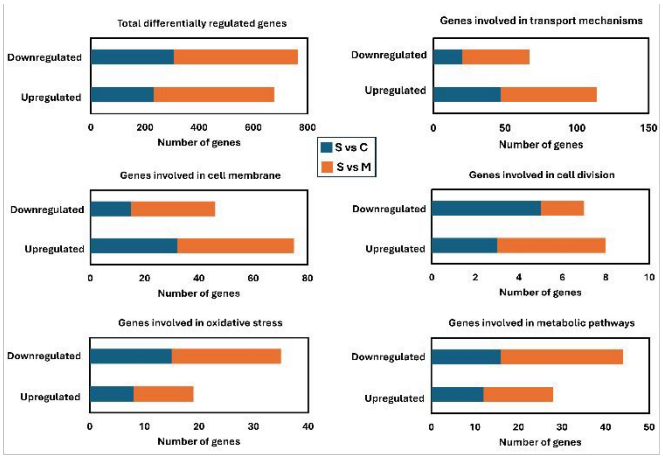

Figure 7. Number of differentially regulated genes that are associated with transport mechanisms, cell division, oxidative stress, cell membrane synthesis and genes involved in various metabolic pathways in *S. mutans* grown on VG surface in compared to control surfaces.

Overall, *S. mutans* cells grown on VG-coated surfaces showed upregulation of a range of genes, which may suggest a potentially complex response to this nanostructured environment. These upregulated genes span multiple functional categories, including amino acid biosynthesis (*argH*, *trpD*, *metB*, *leuB*, *leuC*, *leuD*, *metG*, *metE*), nucleotide metabolism (*guaA*, *pyrR*), and carbohydrate transport and metabolism (*galT*, *lacC*, *lacD*, *lacG*) [54,69,70]. Genes related to protein synthesis and ribosomal function—such as *rplQ*, *rpsK*, *rplE*, *rpmC*, *rplD*, and *rpsJ*—were also upregulated, which may indicate increased translational activity and protein production [71]. Regulatory and stress-response genes, including *nusA*, *hrcA*, *dprA*, and the *brsR/brsM* operon, may indicate a coordinated cellular response that could be involved in managing environmental stress and adjusting gene expression accordingly [72-74]. Upregulation of *lytR* and *lytS*, associated with cell envelope remodelling and signal transduction, and *comGF*, involved in competence development, may further supports this adaptation [52,64]. Moreover, upregulated expression of central metabolic genes such as *acnA*, *icd*, and *citG* suggests metabolic reprogramming, particularly in carbon metabolism pathways [75]. Collectively, these transcriptomic changes reflect a multifaceted physiological response that could contribute to *S. mutans*' survival, metabolic flexibility, and potential virulence on VG-coated surfaces.

In contrast, several genes were notably downregulated in *S. mutans* cells grown on VG-coated surfaces, which may suggest a possible reduction in the activity of certain cellular functions. These include genes involved in transcription and DNA replication, such as *rpoE*, *nusB*, *polA*, and *dnaX*, indicating reduced global gene expression and replication activity [76-78]. Genes related to stress response and protein folding—*groL*, *htpX*, *dpr*, and *rpmF*—were also downregulated, possibly reflecting altered protein quality control under the conditions imposed by VG surfaces [79-81]. When stress response genes are downregulated, the cell's ability to neutralize ROS may be impaired, potentially contributing to elevated oxidative stress. In turn, the excess ROS could damage regulatory proteins, which may further suppress the expression of stress response genes. Additionally, repression of genes involved in metal ion homeostasis (*copZ*), sulfur metabolism (*sufD*), and glutathione synthesis (*gshAB*) may suggest possible shifts in redox regulation and oxidative stress response [81-83]. Carbohydrate metabolism and storage genes (*glgA*, *glgB*, *glgD*, *budA*), as well as amino acid biosynthesis genes (*hisE*, *hisI*, *hisF*), were also suppressed, which may indicate a possible reprioritization of metabolic resources [84-86]. Notably, genes encoding cell division and membrane-associated proteins (*gpsB*, *pbp2b*, *lepB*, *raiA*), along with key regulatory genes like *sloR* and *hdrM*, were downregulated, which may suggest broader effects on cell envelope integrity and transcriptional control [61,87-89].

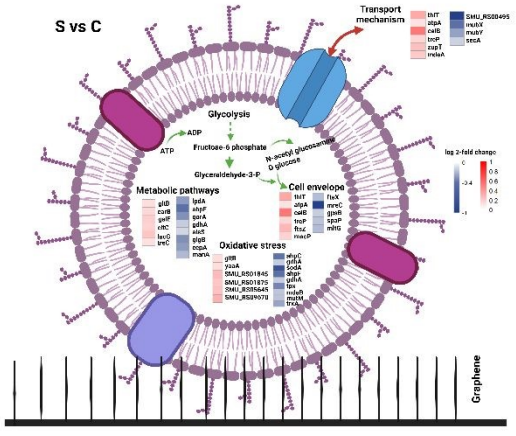

Figure 8. Schematic illustration depicting interaction of VG-coatings to *S. mutans* cell in compared to cells on non-coated surface (S vs C), along with an overview of affected cellular mechanisms, cell envelope, and stress-related responses.

View Article Online
DOI: 10.1039/D6TB00324A

As expected, a greater number of genes were differentially expressed in *S. mutans* cells grown on VG-coated surfaces compared to planktonic cells than between VG-coated and uncoated control surfaces. This is consistent with the well-established physiological differences between planktonic and biofilm-associated cells, which experience distinct environmental cues and mechanical constraints. Among the genes significantly upregulated in cells grown in VG-surface (S) relative to planktonic cells (M) were those involved in translation and ribosome assembly (*infC*, *prfA*, *rsfS*, *rpmJ*, *rpsH*, *rplC*), which may suggest increased protein synthesis [90]. Stress response and protein folding genes (*grpE*, *def*) were also upregulated, which may indicate a potential response to surface-associated stress [91]. Metabolic and regulatory genes—including *trpE* and *guaB* (amino acid and nucleotide metabolism), *cls* (membrane biosynthesis), and *nmlR*, *sppR*, and *aguA* (transcriptional regulation)—also showed increased expression, which may indicate a broader physiological shift [54,84,92]. Upregulation of hypothetical or poorly characterized genes such as *yqeK* and *yqeH* may suggest the involvement of functions that are not yet well understood and could potentially be related to surface colonization. Conversely, several genes were distinctly downregulated in *S. mutans* cells on VG-coated surfaces relative to planktonic cells, which may further reflect a physiological transition toward a more biofilm-like state. These included genes involved in amino acid biosynthesis and metabolism (*thrC*, *metK*, *ilvD*), which may indicate a reduced demand for de novo synthesis [93,94]. Downregulation of *atpD*, a component of the ATP synthase complex, may suggest changes in energy metabolism, potentially reflecting altered or more efficient energy utilization under surface-associated growth conditions [53]. Genes involved in DNA repair and recombination (*recU*, *uvrB*) were also suppressed, which may imply a reduced requirement for DNA maintenance under biofilm conditions [95]. Metabolic genes such as *pflB* (pyruvate formate-lyase) and *fruA* (fructose transporter) were also repressed, which may suggest an altered carbon utilization [96]. Finally, downregulation of global transcriptional regulators such as *purR* and *ciaR* may indicate a broader shift in gene regulatory networks [97].

Together, these findings indicate a complex, surface-specific transcriptional reprogramming in *S. mutans* exposed to VG-coated surfaces. The observed adaptations may help improve survival, adjust metabolic priorities, and modulate stress responses in response to the antimicrobial and mechanical pressures exerted by the nanostructured surface.

VG coating is harmless to osteoblast cells

As shown in Fig. 9A, MG63 cells exhibited comparable fluorescence intensities on both VG-coated and control surfaces, indicating similar levels of metabolic activity and suggesting that the VG coating does not adversely affect cell viability. This was further supported by SEM analysis (Fig. 9B), which indicated similar cell density and morphology across both surfaces, indicating healthy attachment and proliferation.

A similar outcome was observed with HOB cells. Viability data (Fig. S9A) and SEM images (Fig. S9B) indicated no significant differences in cell adhesion, morphology, or proliferation between VG-coated and control surfaces. These findings collectively indicate the good cytocompatibility of VG coatings with osteoblasts, irrespective of cell type, and support their potential for use in bone-contacting biomedical applications.

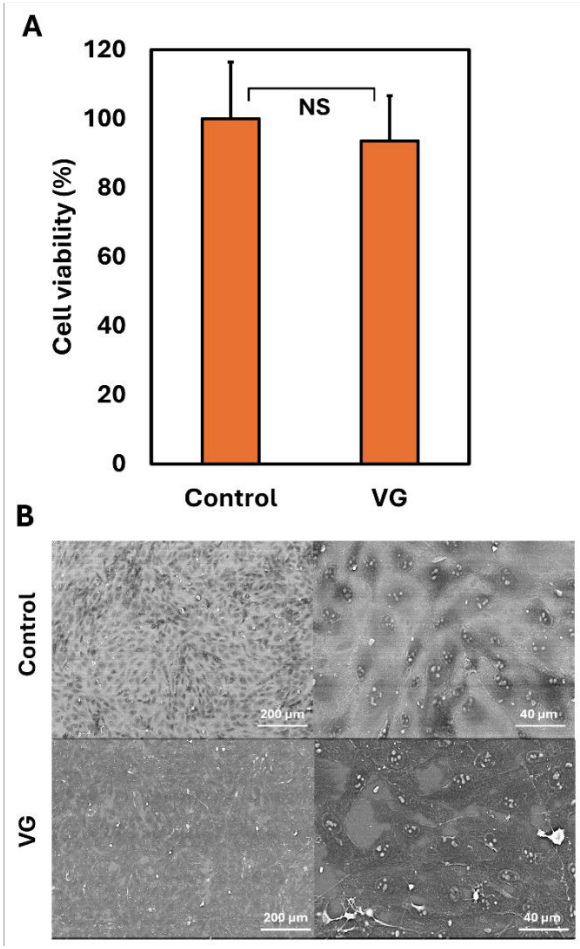

Figure 9. Biocompatibility of VG coated surfaces. Viability of osteosarcoma (MG-63) cells on control and VG coated surfaces after 48 h of growth (A). Representative SEM images of cells on the control and VG coated surfaces (B). NS: not significant (p>0.05).

Conclusions

This study presents the potent antimicrobial efficacy of VG nanoflake coatings against *S. mutans*, a key early colonizer implicated in biofilm formation on dental implant surfaces. The sharp, VG nanostructures significantly reduced bacterial adhesion, viability, and biofilm formation, even in the presence of sucrose, which typically promotes robust EPS production. SEM and confocal microscopy analyses indicated bacterial membrane damage and reduced EPS matrix development on VG-coated surfaces, supporting the hypothesis that VG induces mechano-bactericidal effects through direct membrane disruption. Transcriptomic profiling provided further mechanistic insight, indicating wide alterations in gene expression in response to VG surfaces. Upregulation of genes involved in stress response, translation, and central metabolism may indicate a potential adaptive shift related to survival under surface-imposed mechanical and oxidative stress. Conversely, downregulation of genes related to cell division, membrane biosynthesis, oxidative stress defense, and metabolic activity reflects a potentially altered physiological state and possible reduction in virulence potential in *S. mutans*.

Collectively, these findings indicate that VG coatings, which combine mechanical bactericidal effects with potential metabolic interference, may represent a promising approach for addressing implant-associated infections. The reported biocompatibility of VG surfaces with osteoblasts further supports their potential for use in next-generation biomedical implants with antimicrobial properties and improved osseointegration. However, it is important to note that this study relies on a static droplet mono-species biofilm model, which, despite efforts to control evaporation, has inherent limitations. Specifically, this model does not replicate nutrient gradients, fluid flow, or the complex multispecies interactions typical of clinical biofilms, limiting the direct translational relevance of the results. Therefore, future studies should employ multispecies biofilm models under dynamic flow conditions and evaluate long-term in vivo performance and host immune responses to more rigorously assess the clinical applicability of VG nanostructured coatings.

View Article Online
DOI: 10.1039/D6TB00324A

Author contributions

Xin Chen: Writing, Investigation, Formal analysis. Jian Zhang: Writing – review & editing, Investigation. Shadi Rahimi: Writing, Investigation. Katja Kozjek: Analysis of RNA sequencing. Lena Larsson: Writing – review & editing, Ivan Mijakovic: Supervision, Funding acquisition. Santosh Pandit: Conceptualization, Writing – review & editing, Supervision, Funding acquisition.

Conflicts of interest

There are no conflicts to declare.

Data availability

Data is available within the article and its supplementary materials. The raw RNA-seq data are available in the Genome Expression Omnibus (GEO) database (https://www.ncbi.nlm.nih.gov) under BioProject ID: PRJNA1390808. The other data will be made available by the corresponding author upon reasonable request.

Acknowledgements

This work was supported by grants from Vetenskapsrådet (2020-04096), VINNOVA (2023-04134) to SP and NNF (NNF20CC0035580) to IM. Part of this work was carried out in Chalmers Materials Analysis Laboratory (CMAL). The authors acknowledge the SNP&SEQ Technology Platform National Genomics Infrastructure (NGI) Science for Life Laboratory Uppsala University and National Bioinformatics Infrastructure (NBIS) Sweden for their support in RNA sequencing and data analysis. The data handling was enabled by resources in project naiss2024-23-66 provided by the National Academic Infrastructure for Supercomputing in Sweden (NAISS) at UPPMAX, funded by the Swedish Research Council through grant agreement no. 2022-06725.

Notes and references

1. J. Sahoo, S. Sarkhel, N. Mukherjee and A. Jaiswal, *ACS omega*, 2022, **7**, 45962-45980.
2. A. Trampuz and W. Zimmerli, *Injury*, 2006, **37**, S59-S66.

3. S. Cometta, D.W. Hutmacher and L. Chai, *Biomaterials*, 2024, **309**, 122578.
4. H.C. Flemming and J. Wingender, *Nat. Rev. Microbiol.*, 2010, **8**, 623–33.
5. I. Guzmán-Soto, C. McTiernan, M. Gonzalez-Gomez, A. Ross, K. Gupta, E.J. Suuronen, T.F. Mah, M. Griffith and E.I. Alarcon, *Iscience*, 2021, **24**,102443.
6. V. Nandakumar, S. Chittaranjan, V.M. Kurian and M. Doble, *Polym. J.*, 2013, **45**, 137-152.
7. C.R. Arciola, D. Campoccia and L. Montanaro, *Nat. Rev. Microbiol*., 2018, **16**, 397-409.
8. S. Sharif and A.K. Yadav, *The Microbe*, 2025, 100356.
9. D. Sharma, L. Misba and A.U. Khan, *Antimicrob. Resist. Infect. Control*, 2019, **8**, 76.
10. H.Y. Liu, E.L. Prentice and M.A. Webber, *npj antimicrob. resist.* 2024, **2**, 27.
11. J. Quinn, R. McFadden, C.W. Chan and L. Carson, *IScience*, 2020, **23**, 11.
12. P. Yuan, M. Chen, X. Lu, H. Yang, L. Wang, B. Tian, W. Zhou, T. Liu and S. Yu, *J. Mater. Chem. B*, 2024, 12, 10516-10549.
13. M.C. Cortizo, T.G. Oberti, M.S. Cortizo, A.M. Cortizo and M.A.F.L. de Mele, *J. Dent.* 2012, **40**, 329-337.
14. M. Thukkaram, M. Vaidulych, O. Kylián, J. Hanuš, P. Rigole, S. Aliakbarshirazi, M. Asadian, A. Nikiforov, A. Van Tongel, H. Biederman, T. Coenye, G. Du Laing, R. Morent, L. De Wilde, K. Verbeken and N. De Geyter, *ACS Appl. Mater. Interfaces*, 2020, **12**, 23655-23666.
15. K.V. Holmberg, M. Abdolhosseini, Y. Li, X. Chen, S.U. Gorr and C. Aparicio, *Acta Biomater.,* 2013, **9**, 8224-8231.
16. Y. Yao, P. Lin, D. Ye, H. Miao, L. Cao, P. Zhang, J. Xu and L. Dai, *Int. J. Nanomedicine*, 2025, **20**, 3749-3764.
17. Y. Jiao, L.N. Niu, S. Ma, J. Li, F.R. Tay and J.H. Chen, *Prog. Polym. Sci*., 2017, **71**, 53-90.
18. L. Cheng, K. Zhang, N. Zhang, M.A.S. Melo, M.D. Weir, X.D. Zhou, Y.X. Bai, M.A. Raynolds and H.H.K. Xu, *J. Dent. Res*., 2017, **96**, 855-863.
19. C.Z. Abid, S. Jain, R. Jackeray, S. Chattopadhyay and H. Singh, *J. Biomed. Mater. Res. B Appl. Biomater*., 2017, **105**, 521-530.
20. S. Mohapatra, L. Yutao, S.G. Goh, C. Ng, Y. Luhua, N.H. Tran and K.Y.H. Gin, *J. Hazard. Mater*., 2023, **445**, 130393.
21. W.A. Arnold, A. Blum, J. Branyan, T.A. Bruton, C.C. Carignan, G. Cortopassi, et al., W. A. Arnold, A. Blum, J. Branyan, T. A. Bruton, C. C. Carignan, G. Cortopassi, S. Datta, J. Dewitt, A. Doherty, R. U. Halden, H. Harari, E. M. Hartmann, T. C. Hrubec, S. Iyer, C. F. Kwiatkowski, J. Lapier, D. Li, L. Li, J. G. Muñiz Ortiz, A. Salamova, T. Schettler, R. P. Seguin, A. Soehl, R. Sutton, L. Xu and G. Zheng, *Environ. Sci. Technol*., 2023, **57**, 7645-7665.
22. S.M. Kelleher, O. Habimana, J. Lawler, B. O'Rilly, S. Daniels, E. Casey and A. Cowley, *ACS Appl. Mater. Interfaces*, 2016, **8**, 14966–14974.
23. D.E. Mainwaring, S.H. Nguyen, H. Webb, T. Jakubov, M. Tobin, R.N. Lamb, A.H.F. Wu, R. Marchant, R.J. Crawford and E.P. Ivanova, *Nanoscale*, 2016, **8**, 6527–6534.
24. T. Sjöström, A.H. Nobbs and B. Su, *Mater. Lett*., 2016, **167**, 22-26.
25. G. Hazell, P.W. May, P. Taylor, A.H. Nobbs, C.C. Welch and B. Su, *Biomater. Sci*., 2018, **6**, 1424-1432.
26. N. Rousseau, I. Msolli, P. Chabrand, A. Destainville, O. Richart and J.L. Milan, *J. Periodontal Res*., 2021, **56**, 789-803.
27. R. Li, S. Li, Y. Zhang, D. Jin, Z. Lin, X. Tao, T. Chen, L. Zheng, Z. Zhang and Q. Wu, *Front. bioeng. biotechnol.*, 2023, **11**, 1223339.
28. T. Ziegelmeyer, K.M. de Sousa, T.Y. Liao, R. Lartizien, A. Delay, J. Vollaire, V. Josserand, D. Linklater, P. H. Le, J. L. Coll, G. Bettega, E. P. Ivanova and V. Martel-Frachet, *Mater. Today Bio*, 2025, **32**, 101710.
29. S. Pandit, Z. Cao, V.R.S.S. Mokkapati, E. Celauro, A. Yurgens, M. Lovmar, F. Westerlund, J. Sun and I. Mijakovic, *Adv. Mater. Interfaces*, 2018, **5**, 1701331.
30. S. Pandit, K. Gaska, V.R.S.S Mokkapati, E. Celauro, A. Derouiche, S. Forsberg, M. Svensson, R. Kádár and I. Mijakovic, *Small*, 2020, **16**, 1904756.
31. Y. Chen, S. Pandit, S. Rahimi and I. Mijakovic, *Carbon*, 2024, **218**, 118740.
32. W. Wei, J. Li, Z. Liu, Y. Deng, D. Chen, P. Gu, G. Wang and X. Fan, *J. Mater. Chem. B*, 2020, **8**, 6069-6079.
33. S. Pandit, M.A. Kim, J.E. Jung, H.M. Choi and J.G. Jeon, *Biofilm*, 2024, 8, 100241.

34. A. Heydorn, A.T. Nielsen, M. Hentzer, C. Sternberg, M. Givskov, B.K. Ersbøll and S. Molin, *Microbiology*, 2000, **146**, 2395-2407.
35. P.A. Ewels, A. Peltzer, S. Fillinger, H. Patel, J. Alneberg, A. Wilm, M.U. Garcia, P.D. Tommaso and S. Nahnsen, *Nat. Biotechnol*., 2020, **38**, 276-278.
36. H. Patel, P. Ewels, A. Peltzer, O. Botvinnik, G. Sturm, D. Moreno, P. Vemuri, M. U. Garcia, Silviamorins , L. Pantano, ; M. Binzer-Panchal, N. C. Bot, R. Syme, M. Zepper, G. Kelly, F. Hanssen, Y. J. A. Fellows, C. Cheshire, Rfenouil, J. Espinosa-Carrasco, Marchoeppner , E. Miller, A. Talbot, P. Zhou, S. Guinchard, M. Hörtenhuber, G. Gabernet, C. Mertes, D. Straub and P. D. Tommaso, *Zenodo*, 2023.
37. A. Dobin, C.A. Davis, F. Schlesinger, J. Drenkow, C. Zaleski, S. Jha, P. Batut, M. Chaisson, T.R. Gingeras, *Bioinformatics,* 2013, **29**, 15-21.
38. Y. Liao, G.K. Smyth and W. Shi, *Bioinformatics*, 2014, **30**, 923-930.
39. M.I. Love, W. Huber and S. Anders, *Genome Biol*., 2014, **15**, 550.
40. Z. Xie, A. Bailey, M. V. Kuleshov, D. J. B. Clarke, J. E. Evangelista, S. L. Jenkins, A. Lachmann, M. L. Wojciechowicz, E. Kropiwnicki, K. M. Jagodnik, M. Jeon and A. Ma'ayan, *Curr. Protoc*., 2021, **1**, e90.
41. Y. Wei, G.P. Dang, Z.Y. Ren, M.C. Wan, C.Y. Wang, H.B. Li, T. Zhang, F.R. Tay and L. N. Niu, *NPJ Bionfilms Microbi*., 2024,**10**, 56.
42. M. Feldman, W.S. Moustafa Elsayed, M. Friedman, I. Gati, D. Steinberg and H. Marei, *Int. J. Dent.*, 2022(1), 7246155.
43. A.S. Meza-Siccha, M.A. Aguilar-Luis, W. Silva-Caso, F. Mazulis, C. Barragan-Salazar and J. del Valle-Mendoza, *Int. J. Dent.*, 2019(1), 4292976.
44. J.A. Lemos, S.R. Palmer, L. Zeng, Z.T. Wen, J.K. Kajfasz, I.A. Freires, J. Abranches and L.J. Brady, *Microbiol. Spectr.*, 2019, **7**,10-1128.
45. H. Koo, J. Xiao, M.I. Klein and J.G. Jeon, *J. Bacteriol.*, 2010, **192**, 3024-3032.
46. Q. Zhang, Q. Ma, Y. Wang, H. Wu and J. Zou, *Int. J. Oral Sci.,* 2021, **13**, 30.
47. Y. Tu, M. Lv, P. Xiu, T. Huynh, M. Zhang, M. Castelli, Z. Liu, Q. Huang, C. Fan, H. Fang and R. Zhou, *Nat. Nanotechnol.,* 2013, **8**, 594-601.
48. D.P. Linklater, V.A. Baulin, S. Juodkazis and E.P. Ivanova, *Interface Focus*, 2018, **8**, 20170060.
49. S. Liu, T.H. Zeng, M. Hofmann, E. Burcombe, J. Wei, R. Jiang, J. Kong and Y. Chen, *ACS nano*, 2011, **5**, 6971-6980.
50. N. Parvin, S.W. Joo and T.K. Mandal, *Antibiotics*, 2025, **14**, 207.
51. M. Shemesh, A. Tam and D. Steinberg, *Microbiology*, 2007, **153**, 1307-1317.
52. M. Afzal, M. Carda-Diéguez, S. Bloch, L.G. Thies, A. Mira and C. Schäffer, *Front. oral health*, 2025, **6**, 1535034.
53. M.I. Klein, J. Xiao, B. Lu, C.M. Delahunty, J. R. Yates III and H. Koo, *Plos One*, 2012, **7**, e45795.
54. D. Dufour, H. Li, S.G. Gong and C.M. Lévesque, *Genes*, 2023, **14**, 1887.
55. Y. Chen, Y. Li, C. Yuan, S. Liu, F. Xin, X. Deng and X. Wang, *Mol. Oral Microbiol.*, 2022, 37, 97-108.
56. K. Moon, S. Hwang, H.J. Lee, E. Jo, J.N. Kim and J. Cha, *Front. microbiol*., 2022, **13**, 945023.
57. Y. Li, D. Qiao, Y. Zhang, W. Hao, Y. Xi, X. Deng, X. Ge and M. Xu, *Mol. Oral Microbiol.*, 2021, **36**, 295-307.
58. R. Nagasawa, T. Sato, N. Nomura, T. Nakamura and H. Senpuku, *Appl. Environ. Microbiol*., 2020, **86**, e00770-20.
59. L.A. Vega, M. Sanson-Iglesias, P. Mukherjee, K.D. Buchan, G. Morrison, A.E. Hohlt and A.R. Flores, *Antimicrob. Agents Chemother.*, 2024, **68**, e00496-24.
60. H.C.T. Tsui, J.J. Zheng, A.N. Magallon, J.D. Ryan, R. Yunck, B.E. Rued, T.G. Bernhardt and M.E. Winkler, *Mol. Microbiol*., 2016, **100**, 1039-1065.
61. L.R. Hammond, M.D. Sacco, S.J. Khan, C. Spanoudis, A. Hough-Neidig, Y. Chen and P.J. Eswara, *Microbiol. Spectr.*, 2022, **10**, e01413-22.
62. A. Galinier, C. Delan-Forino, E. Foulquier, H. Lakhal and F. Pompeo, *Biomolecules*, 2023, **13**, 720.
63. Z.T. Wen, D. Yates, S.J. Ahn and R.A. Burne, *BMC Microbiol*., 2010, **10**, 111.
64. J.P. Bitoun, S. Liao, X. Yao, S.J. Ahn, R. Isoda, A.H. Nguyen, L.J. Brady, R.A. Burne, J. Abranches and Z.T. Wen, *Appl. Environ. Microbiol*., 2012, **78**, 2914-2922.
65. J.K. Kajfasz, T. Ganguly, E.L. Hardin, J. Abranches and J.A. Lemos, *Sci. Rep.*, 2017, **7**, 16018.
66. J. Liu, C. Wu, I.H. Huang, J. Merritt and F. Qi, *Microbiology*, 2011, **157**, 2433-2444.

67. J.L. Baker, J. Abranches, R.C. Faustoferri, C.J. Hubbard, J.A. Lemos, M.A. Courtney and R. Quivey Jr, *Mol. Oral Microbiol*., 2015, **30**, 496-517.
68. J. Abranches, M.M. Nascimento, L. Zeng, C.M. Browngardt, Z.T. Wen, M. F. Rivera and R.A. Burne, *J. Bacteriol*., 2008, **190**, 2340-2349.
69. J. Kong, K. Xia, X. Su, X. Zheng, C. Diao, X. Yang, X. Zuo, J. Xu and X. Liang, *AMB Express*, 2021, **11**, 102.
70. M. Jing, T. Zheng, T. Gong, J. Yan, J. Chen, Y. Lin, B. Tang, Q. Ma, X. Zhou and Y. Li, *Microbiol. Spectr.*, 2022, 10, e00721-22.
71. C. Eymann, G. Homuth, C. Scharf and M. Hecker, *J. Bacteriol*., 2002, **184**, 2500-2520.
72. J.A. Lemos, Y.Y.M. Chen and R.A. Burne, *J. Bacteriol*., 2001, **183**, 6074-6084.
73. Z. Xie, T. Okinaga, G. Niu, F. Qi and J. Merritt, *Mol. Microbiol*., 2010, **78**, 1431-1447.
74. K. Fujishima, M. Kawada-Matsuo, Y. Oogai, M. Tokuda, M. Torii and H. Komatsuzawa, *Appl. Environ. Microbiol.*, 2013, **79**, 1436-1443.
75. J.S. Chia, Y.Y. Lee, P.T. Huang and J.Y. Chen, *Infect. Immun.*, 2001, **69**, 2493-2501.
76. X. Xue, J. Tomasch, H. Sztajer and I. Wagner-Döbler, *J. Bacteriol*., 2010, **192**, 5081-5092.
77. A.C. Len, D.W. Harty and N.A. Jacques, *Microbiology*, 2004, **150**, 1339-1351.
78. M.W. Sherman, S. Sandeep and L.M. Contreras, *ACS Synth. Biol.,* 2021, **10**, 1024-1038.
79. Z.T. Wen, P. Suntharaligham, D.G. Cvitkovitch and R.A. Burne, *Infect. Immun*., 2005, **73**, 219-225.
80. A.C. Len, D.W. Harty and N.A. Jacques, *Microbiology*, 2004, **150**, 1339-1351.
81. X. Cheng, X. Xu, X. Zhou and J. Ning, *J. Oral Microbiol.,* 2024, **16**, 2292539.
82. S.S. Garcia, Q. Du and H. Wu, *Mol. Oral Microbiol*., 2016, **31**, 515-525.
83. K. Ellepola, X. Huang, R.P. Riley, J.P. Bitoun and Z.T. Wen, Front. microbiol., 2021, **12**, 671533.
84. B.E. Costa Oliveira, A.P. Ricomini Filho, R.A. Burne and L. Zeng, *Front. microbiol*., 2021, **12**, 636684.
85. Z.D. Moye, L. Zeng and R.A. Burne, *Appl. Environ. Microbiol*., 2014, **80**, 972-985.
86. L. Yang, Y. Chen, Y. Chi, X. Chen, Y. Zhao, M. Zhang, X. Wang, Y. Li, J. Nie and X. Wang, *J. Oral Microbiol.*, 2025, **17**, 2533174.
87. F. Pompeo, E. Foulquier, B. Serrano, C. Grangeasse and A. Galinier, *Mol. Microbiol*., 2015, **97**, 139-150.
88. Tsui, H.C.T., Boersma, M.J., Vella, S.A., Kocaoglu, O., Kuru, E., Peceny, J.K., E.E. Carlson, M.S. VanNieuwenhze, Y.V. Brun, S.L. Shaw and M.E. Winkler, *Mol. Microbiol.*, 2014, **94**, 21-40.
89. K.P. O'Rourke, J.D. Shaw, M.W. Pesesky, B.T. Cook, S.M. Roberts, J.P. Bond and G.A. Spatafora, *J. Bacteriol*., 2010, **192**, 1433-1443.
90. P. Treerat, C. de Mattos, M. Burnside, H. Zhang, Y. Zhu, Z. Zou, D. Anderson, H. Wu, J. Merritt and J. Kreth, *J. Bacteriol*., 2024, **206**, e00104-24.
91. J.A. Lemos, Y. Luzardo and R.A. Burne, *J. Bacteriol.*, 2007, **189**, 1582-1588.
92. M.E. MacGilvray, J.D. Lapek Jr, A.E. Friedman and R.G. Quivey Jr, *Microbiology*, 2012, **158**, 2133-2143.
93. B. Santiago, M. Marek, R.C. Faustoferri and R.G. Quivey Jr, *J. Bacteriol*., 2013, **195**, 3552-3562.
94. G.A. Ashniev, S.N. Petrov and S.N. Iablokov, *Microorganisms*, 2022, **10**, 740.
95. M.I. Klein, L. DeBaz, S. Agidi, H. Lee, G. Xie, A.H.M. Lin, B.R. Hamaker, J.A. Lemos and H. Koo, *PloS one*, 2010, **5**, e13478.
96. L. Zeng, Z.T. Wen and R.A. Burne, *Mol. Microbiol*., 2006, **62**, 187-200.
97. C. Wu, E.A. Ayala, J.S. Downey, J. Merritt, S.D. Goodman and F. Qi, *J. Bacteriol*., 2010, **192**, 4669-4679.

View Article Online
DOI: 10.1039/D6TB00324A

View Article Online
DOI: 10.1039/D6TB00324A

Data availability

Data is available within the article and its supplementary materials. The raw RNA-seq data are available in the Genome Expression Omnibus (GEO) database (https://www.ncbi.nlm.nih.gov) under BioProject ID: PRJNA1390808. The other data will be made available by the corresponding author upon reasonable request.